Research article

Z-scheme NiO/g-C$_3$N$_4$ nanocomposites prepared using phyto-mediated nickel nanoparticles for the efficient photocatalytic degradation

Is Fatimah [a,*], Rizky Zenita Sulistyowati [a], Adytia Wijayana [a], Gani Purwiandono [a], Suresh Sagadevan [b]

[a] *Department of Chemistry, Faculty of Mathematics and Natural Sciences, Universitas Islam Indonesia, Kampus Terpadu UII, Jl. Kaliurang Km 14, Sleman, Yogyakarta, Indonesia*
[b] *Nanotechnology and Catalysis Research Center (NANOCAT), Universiti Malaya, Level 3 Block A, 50603 Kuala Lumpur, Federal Territory of Kuala Lumpur, Malaysia*

ARTICLE INFO

ABSTRACT

Highly-effective photocatalyst of NiO/g-C$_3$N$_4$ with was successfully synthesized by using phyto-mediated-synthesized nickel nanoparticles. The preparation was initiated by synthesizing nickel nanoparticles by using *Tinosphora cordifolia* stem extract under ultrasound-assisted method followed by the dispersing onto g-C$_3$N$_4$ structure. The study focused on physicochemical characterization and photocatalytic activity as function of the percentage of Ni in the nanocomposite. The photocatalytic activity examinations were carried out to rhodamine B and tetracycline photocatalytic oxidation. The results demonstrated that graphitic carbon nitride is effectively improved the photocatalytic activity of NiO for both photocatalytic oxidation reactions. From the varied Ni content of 5; 10; and 20 %wt., it was also found that the highest photoactivity was achieved by the composite having 10 %wt. of nickel content. The high effectivity was showed by degradation efficiency of 95% toward Rhodamine B and 98% toward tetracycline. The examination on effect of scavengers suggests that Z-scheme involved in the photocatalytic mechanism which facilitated the efficient separation of the photogenerated electron–hole pairs under visible light illumination. In summary, the present findings provide a green approach for fabricating the effective photocatalysts for organic contaminant degradation.

1. Introduction

The release of large number of dyes and antibiotics-containing wastewater from various industrial and medical activities to the environment is one of the serious problems in environmental sanitation. In fact, the use of huge number of dyes has created the development in many products such from printing, textile, pigment technologies, but during the industrial process, it is more than 10% of the dyes released as waste [1]. As similar with the dyes, antibiotic-contaminated wastewater must be released from the pharmaceutical industries. Such wastewater release requires a sophisticated technology for removal before releasing to water bodies. Advanced oxidation processes (AOPs) including photocatalytic oxidation mechanism is well-known technology for organic

---

* Corresponding author.
E-mail address: isfatimah@uii.ac.id (I. Fatimah).

contaminated-water treatment [2]. Such organic compounds of dye, pharmaceuticals including antibiotics and other aromatic compounds are the serious target of wastewater treatment in vast industrial area. Within the scheme, the oxidation process could be conducted via photocatalysis, piezocatalysis, ozonization, wet peroxidation, etc. [3,4]. For the effectiveness of the industrial process, designing effective photocatalyst with high stability, reusability, and capability to work in wide range of light have been attempted [5].

With smaller band gap energy (2.6 eV), graphitic carbon nitride (g-C$_3$N$_4$) has attracted great attentions. Its combinations with some metal oxide photocatalysts in the nanocomposite formation have been attempted to improve photocatalytic efficiency [6]. The possible heterojunction gives the advantages to reduce recombination rate. With this scheme, the combination of NiO nanoparticles (NiO NPs) with g-C$_3$N$_4$ has been proven to have enhanced photocatalytic capability in visible light region [7]. By the combination of the band gap energy of both NiO NPs and g-C$_3$N$_4$, a Z-scheme photocatalytic mechanism could be reached as a strategy to enhance photocatalytic efficiency. Based on many previous works, the mechanism will give benefit regarding to the turnover frequency of photocatalysis, including the activity in photocatalytic degradation of dye molecule.

In other side, the green approaches in the synthesis of NPs are also intensively studied in the green chemistry perspective. The use of phytochemicals-mediated reduction of metal precursor is valued as safer and get much interests. Such plants extracts containing secondary metabolites were valued as effective bioreductor with the additional function as capping agent of the nanoparticles [8]. A lot of interests have been expressed from the use of some plant's extracts, and in addition, the studies toward controlling the particle size and shape of the nanostructures by manipulating reaction parameters. The effectiveness of biosynthesized NiO NPs as catalyst and photocatalyst has been reported for removal of many organic contaminants. *Tinosphora cordifolia* is one of the popular traditional medicinal plants from Asian countries [9,10]. The functionality of the plant's extract as anticancer, antibacterial, etc. is consequently related with the high content of secondary metabolites such as flavon, flavanol, and flavonoids in the extract [11,12]. The *Tinosphora cordifolia* stem extract (TCE) has been reported to be effective in the biosynthesis of Ag NPs, CuO NPs, and SnO$_2$ NPs [13–15].

Based on these backgrounds, Z-scheme NiO/g-C$_3$N$_4$ nanocomposites was synthesized by using TCE as bioreductor, and the material was tested as photocatalyst for the degradation of dye molecule, rhodamine B (RhB) and antibiotic of tetracycline (TC). Research was aimed to study the physicochemical properties and photocatalytic activity of the prepared material. Rh B was chosen as dye molecule due to its vast utilization in many industries such textile, ink and printing, paint, etc, meanwhile TC is a popular pharmaceutic which its controlling and monitoring in environment need to be seriously taken. The advantages of the method utilized in this work is related with the use of TCE as bioreductor which gives alternative as greener reagent in the synthesis, and in addition, the photocatalytic activity examination on dye molecule will give a perspective for further material's development in wastewater treatment.

2. Materials and method

2.1. Materials

Tinosphora cordifolia steam powder were purchased from traditional market in Sleman District, Yogyakarta Special province, Indonesia. About 10 g of the powder were soaked in 100 mL water for overnight to get *Tinosphora cordifolia* extract (TCE). Chemicals consist of rhodamine B (RhB), tetracycline (TC), NiCl$_2$·6H$_2$O, H$_2$O$_2$, ethylene diamine tetra acetate (EDTA), isopropanol (IPR), and H$_2$SO$_4$ were in pro analyst grade purchased from Merck-Millipore (Germany).

2.2. Preparation of nickel nanoparticles (NiO NPs)

Nickel oxide nanoparticles (NiO NPs) was prepared by previously synthesize Ni NPs by mixing 25 mL of the TCE and 25 mL of 0.1 M of NiCl$_2$·6H$_2$O solution followed by ultrasound irradiation for 15 min. The formation of Ni NPs was evaluated by using UV–Visible spectrophotometry and transmission electron microscope (TEM) analysis. The conversion of Ni NPs into NiO NPs was performed by calcining the Ni NPs solid, which obtained by solvent evaporation. The calcination was at 500 °C for 4 h, with a heating rate of 5 °C. min^{-1}.

2.3. Preparation of NiO/g-C$_3$N$_4$ samples

The g-C$_3$N$_4$ powder was prepared by a facile thermal polycondensation of urea. Typically, 5 g of urea powder was put into a closed crucible and heated at 500 °C in a furnace with a rate of 5 °C.min^{-1} for 4 h [16]. The NiO/g-C$_3$N$_4$ nanocomposites were prepared by a hydrothermal method using prepared g-C$_3$N$_4$, and Ni NPs solution. The method was adopted from the preparation of NiO–ZnO/g-C$_3$N$_4$ which gave high surface area and homogeneous distributed NPs [17]. In a typical procedure, appropriate amount of g-C$_3$N$_4$ powder was added into the solution at the certain Ni concentrations of 5, 10 and 20 % wt. Subsequently, the mixtures were stirred for 30 min before were transferred into a Teflon-lined stainless-steel autoclave. The hydrothermal treatment was applied at the temperature of 150 °C for overnight. Later the product was collected followed by washing with deionized water. The solid was then dried in oven at 80 °C followed by calcination at 400 °C for 2 h. From the varied Ni content of 5, 10, and 20 %wt., the NiO/g-C$_3$N$_4$ samples were encoded as 5Ni/C$_3$N$_4$, 10Ni/C$_3$N$_4$ and 10Ni/C$_3$N$_4$, respectively.

2.4. Physicochemical characterization

Various spectroscopic techniques were applied to analyze the physicochemical properties of prepared NiO NPs and NiO/g-C$_3$N$_4$ samples. The identification of Ni NPs was confirmed using HITACHI U-2080 UV–Vis spectrophotometer (Tokyo, Japan) at scanning

range of 200–800 nm. Fourier transformed infrared spectroscopy (FT-IR) with spectral ranges 400–4000 cm^{-1} were recorded on Nicolet AVATAR instrument to verify the formation of nanocomposite and stabilizing properties of functional groups involved in the synthesis. X-ray powder diffraction (XRD) of the as-prepared g-C$_3$N$_4$ and NiO/g-C$_3$N$_4$ photocatalysts was investigated on a Thermo ARL SCINTAG X'TRA X-ray diffractometer using Cu-Kα radiation (λ = 0.154056 nm). High-resolution transmission electron microscopy (HRTEM, Tecnai G2 F30 S-Twin) was employed to observe the morphology and microstructures of as-prepared samples. The optical absorption properties of the samples were investigated via UV–Vis diffuse reflectance spectroscopy (DRS) using a JASCO V-760 (Tokyo, Japan). The surface analysis of the NiO/g-C$_3$N$_4$ was conducted on a X-ray photoelectron spectroscopy (XPS) analysis using V. G. Scientific ESKALAB MKII (Tokyo, Japan) instrument. For the analysis, a monochromatic Al K_α radiation with a photon energy of 1486.6 ± 0.2 eV was utilized. Electrochemical impedance spectroscopy (EIS) data were collected on an Metrohm Autolab PGSTAT 302 N electrochemical workstation. The electrolyte solution was sodium sulfate aqueous solution, and the electrodes are glassy carbon electrode and nickel foam. Photoluminescence (PL) spectroscopy was monitored using a transient fluorescence spectrometer (Horiba HJY FM- 4 P-TCSPC).

2.5. Photocatalytic experiments

Examination of the photocatalytic activity of NiO/g-C$_3$N$_4$ samples was conducted on RhB and TC photodegradation in a batch reactor equipped with visible light (Xenon Lamp, Philips, 20 W). For a typical reaction, 0.2 g of catalyst was dispersed into 250 mL of the tested solution, and then about 2 mM of H$_2$O$_2$ was added. The kinetics of photodegradation was evaluated by monitoring the concentration of solution by using UV–Vis spectrophotometry analysis, and in order to confirm the degradation, high performance liquid chromatography analysis was performed on the HPLC Waters instrument (Singapore). The degradation efficiency (DE/%) was determined based on following equation (eq. (1)):

$$DE\ (\%) = \frac{C_0 - C_t}{C_0} x100 \tag{1}$$

With C_o and C_t are the initial concentration and the concentration of RhB and TC at time of t, respectively.
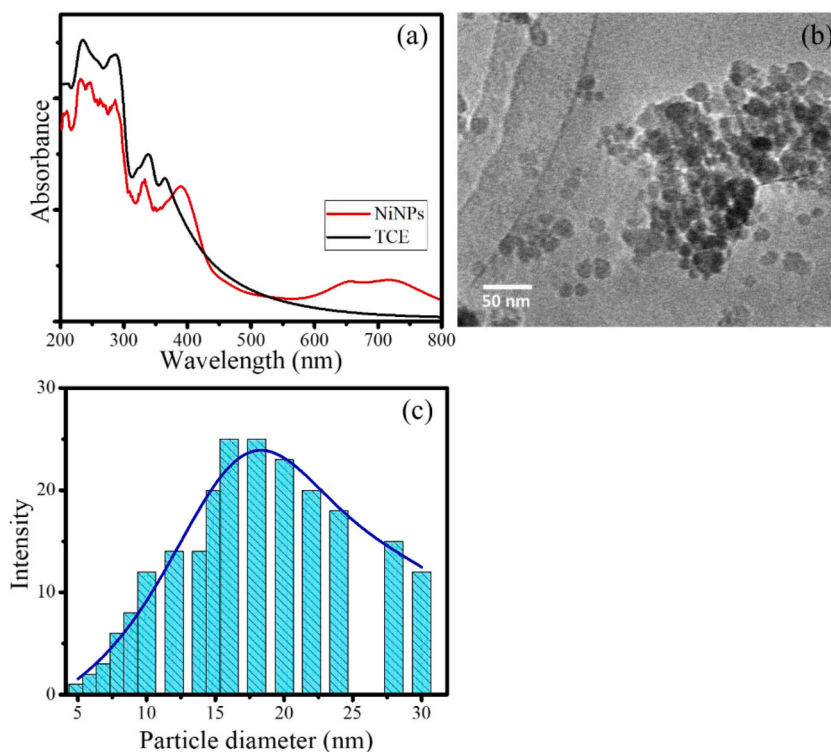
Fig. 1. (a) Comparison on UV–Visible spectra of TCE and Ni NPs, (b) TEM image of Ni NPs, (c) Particle size distribution of Ni NPs.

3. Results and discussion

3.1. Synthesis and characterization

The first and crucial step in the synthesis of NiO/g-C$_3$N$_4$ nanocomposite is the synthesis of Ni NPs by using TCE as bioreductor. The monitoring of the Ni NPs formation was conducted by using UV–Visible spectrophotometry with the spectra in Fig. 1.

The comparison on TCE and Ni NPs spectra revealed the evolution of the solution composition as there is a characteristic peak at 401 nm with additional broad peak at around 500–550 nm. With different appearance, the TCE shows peaks at 250; 290; 320 and 380 nm, that are associated with the presence of high containing flavonoids in the extract [18,19]. Refer to the determination on plasmon resonance spectra, the observed peak at 401 nm is associated with the smaller particle's radii (~7 nm), and in addition the peak at 550 nm is indication for the bigger radii (from 7 to 60 nm) [20–22]. These identifications are in confirmation with the TEM analysis to the Ni NPs solution as depicted in Fig. 1b. It is seen that the irregular spherical forms in range of 10–30 nm are appeared. Refer to previous phytochemical screening remarked that tinocordicide is the dominant component in TCE [23], the reduction mechanism can be described as scheme presented in Fig. 2. The Ni NPs are the particles surrounded by the secondary metabolites that reduced Ni^{2+}, and furthermore the bonded metabolites are the capping agent [24].

As the NiO/g-C$_3$N$_4$ prepared, the structure identification was conducted. Analysis using XRD expressed the reflections in comparison between with g-C$_3$N$_4$ and NiO/g-C$_3$N$_4$ samples and presented in Fig. 3. There are two obvious diffraction peaks around 13.13° and 27.45° that are corresponding to the (100) and (002) planes of g-C$_3$N$_4$ structure, consistent with the standard value (JCPDS 87–1526) [16,25]. These peaks are attributed to the structure of the tri-s-triazine unit with interplanar spacing and the conjugated aromatic system, respectively. Similar pattern of the reflections is exhibited by 5NiO/C$_3$N$_4$ and 10NiO/C$_3$N$_4$, meanwhile the 20NiO/C$_3$N$_4$ demonstrates the additional peaks instead of the characteristic peak of g-C$_3$N$_4$. 20NiO/C$_3$N$_4$ demonstrates sharp diffraction peaks at 37.23, 43.26, and 62.81° which can be respectively indexed to the crystal planes of (1 1 1), (2 0 0), and (2 2 0) of cubical structure of NiO nanoparticles, refer to JCPDS 47–1049 [26,27]. This is in accordance with the reflected peaks of NiO NPs nanocomposite peaks located at same position. The interpretation from these results suggests a homogeneous distributed NiO NPs at low concentration, while at higher concentration, the growth of NiO crystalline is identified. Moreover, the calculated average crystallite sizes of NiO in NiO NPs and 20Ni/C$_3$N$_4$ from the diffraction angle, 2θ of 37.23, 43.26, and 62.81° using Debye-Scherrer equation are 27.6 nm and 39.8 nm, respectively.

Analysis of FTIR to confirm the NiO NPs attachment in the nanocomposite produced the spectra as presented in Fig. 4. In general, the both NiO/C$_3$N$_4$ and g-C$_3$N$_4$ show similar absorptions, suggest that the overall structure of g-C$_3$N$_4$ is maintained as the original form after NiO NPs loading. Such specific peaks at 1638 cm^{-1} are attributed to C=N stretching vibration mode, and in addition, the aromatic C–N bond is expressed by the absorption at around 1205, 1230, 1313, 1459, 1536, and 1571 cm^{-1} [28]. The broad peaks centered at 3089 and 3158 cm^{-1} could be assigned to the stretching mode of the N–H bond. Some associated peaks are in higher number at NiO/g-C$_3$N$_4$ compared to g-C$_3$N$_4$ suggests the NiO bonded to the g-C$_3$N$_4$ support. The occurrence of NiO NPs in the composite is also identified by sharp peak at 600.7 cm^{-1} as characteristics of NiO, which is consistent with that reported elsewhere. The
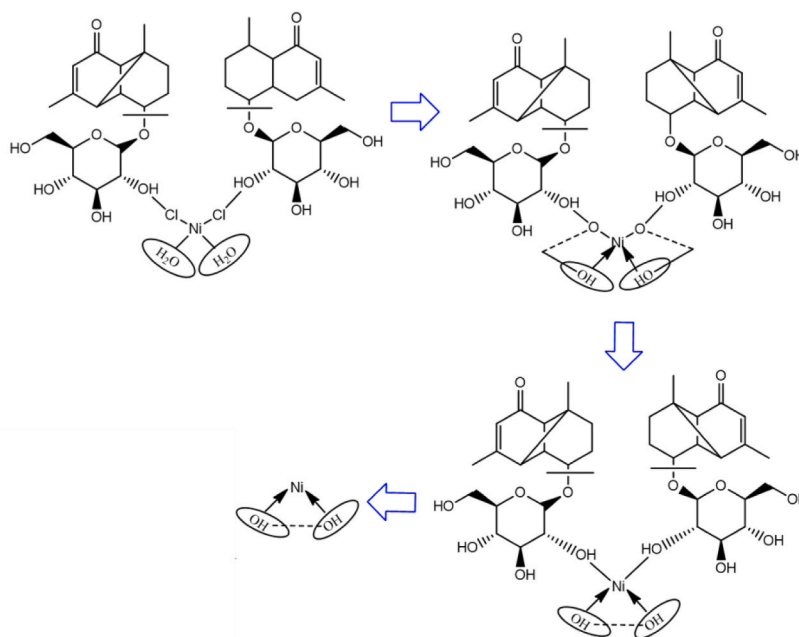

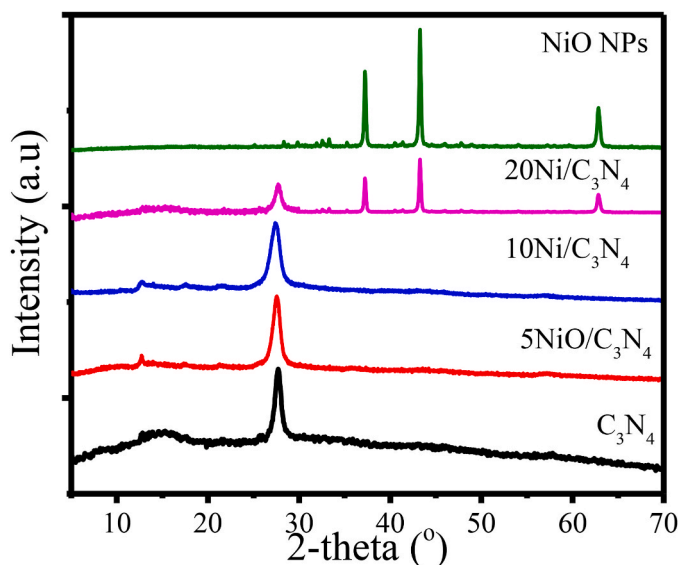**Fig. 2.** Reduction mechanism in Ni NPs formation by using TCE.

Fig. 3. XRD pattern of materials.

confirmation on the presence of NiO nanoparticles is also seen by the comparison with the spectrum of NiO sample. There are some observed peaks 3645 cm^{-1} and 1636.7 cm^{-1} which are associated with the presence of OH from water and possible capping agent. In addition, the absorption at 605.2 cm^{-1} is assigned to the Ni–O stretching band which confirm the formation of NiO nanoparticles.

The evolution of surface profile of the material was analyzed by using SEM analysis with the images presented in Fig. 5. It is seen from Fig. 5a-b that lamellar structure is appeared by the pristine g-C_3N_4 sample, furthermore, after decoration with NiO NPs, it is clearly to be seen from Fig. 5c-f that there is no significant change of the morphology of the surface representing that NiO NPs are evenly distributed on the surface. By comparison on morphologies of Fig. 5c-f, slight porosity change is appeared by NiO dispersion as the 5Ni/C_3N_4 and 20Ni/C_3N_4 exhibit less porosity compared to g-C_3N_4. Moreover, the EDX analysis results are presented in Table 1 confirmed the presence of NiO NPs in the NiO/g-C_3N_4 nanocomposites. It is seen that the suitability of the identified Ni content with the intended Ni content expressed by all NiO/g-C_3N_4 samples as the synthesis method involved direct dispersion of Ni NPs solution onto g-C_3N_4. As can be seen from the elemental mapping of 10Ni/C_3N_4 sample presented in Fig. 6, the elements of Ni, C and N are homogeneously distributed. It represents that the NiO compounds are evenly dispersed in whole nanocomposite.

Moreover, TEM and HRTEM analysis results of NiO/g-C_3N_4 samples depicted in Fig. 7 represent the occurrence of NiO NPs. Fig. 7a–b demonstrate the layered structure of g-C_3N_4, and after NiO dispersion, the particles in irregular forms are appeared (Fig. 7 c). From Fig. 7c, lattice fringes identified in 20Ni/C_3N_4 from HRTEM analysis are with the spacing of 0.25 nm, associated with the (111) spacing of NiO. This is also strengthened by the SAED spectrum (Fig. 7e) demonstrates the (111) and (200) lattices that are associated with calculated d-spacing from XRD reflections analysis.

Surface analysis represents the elemental compositions in NiO/g-C_3N_4 by XPS analysis with the spectra presented in Fig. 8. The XPS survey scan spectrum (Fig. 7a) demonstrates that the sample mainly composed of C, N, Ni and O. The existence of g-C_3N_4 is identified by the deconvoluted N 1s peak XPS spectrum which shows three Gaussian−Lorenzian peaks centered at 399.2, 400.3, and 402.5 eV. The peaks can be attributed to the pyridinic-like nitrogen (N−sp^2 C), graphitic nitrogen (N−(C)3), and amino groups carrying a hydrogen atom (–CN–H). The occurrence of NiO NPs in the nanocomposite is confirmed by the XPS spectrum of NiO which demonstrate the peaks at 873.2 eV and 855.8 eV that are associated with Ni2p3/2 and Ni2p1/2. Moreover, the spin- Ni2p orbital splitting between Ni (2p1/2) and Ni (2p3/2) is calculated of 17.28 eV, with additional satellite peaks at 879.8, 872.2, and 862.5 eV are observed (Fig. 8b). These peaks are in good agreement with those reported earlier for NiO NPs [27,29,30]. It is also strengthened by the deconvoluted C 1s peak which presents two distinct peaks at binding energies of 284.6 eV and 288.2 eV. These peaks are attributed to the sp^2 (C–C bonds) and sp^2 -bonded carbon in (N–C═N) (Fig. 8c and d).

Optical properties of the materials were studied by using UV-DRS analysis. Fig. 8 shows the absorption spectra of the materials. It is seen that g-C_3N_4 expresses the absorption at UV and visible light region, meanwhile NiO NPs shows the absorption spectrum at the UV region (Fig. 9a). The supporting NiO into g-C_3N_4 contributes to the absorption at the visible range. Furthermore, the band gap energy values of the nanocomposites were determined according to the Tauc's plot. From the determined edge wavelength of the plots, the calculated band gap values of g-C_3N_4, 5Ni/C_3N_4, 10Ni/C_3N_4, and 20Ni/C_3N_4 are 2.59; 2.65; 3.10 and 3.00 eV respectively (Fig. 9b). In addition, the band gap energy value of NiO NPs is 3.28 eV. Remarkably, the supporting g-C_3N_4 to NiO NPs decreases the band gap energy which associated with the improved visible light utilization ability. Similar phenomena were reported by the supporting NiO and TiO_2 on g-C_3N_4 support [7,31]. This is fit with the purpose of NiO modification for enabling photocatalyst to absorb light at wider light range as the available light absorption of the photocatalyst increases, the generation of photogenerated electrons will be more conducive, so it will give a better photocatalytic effect.
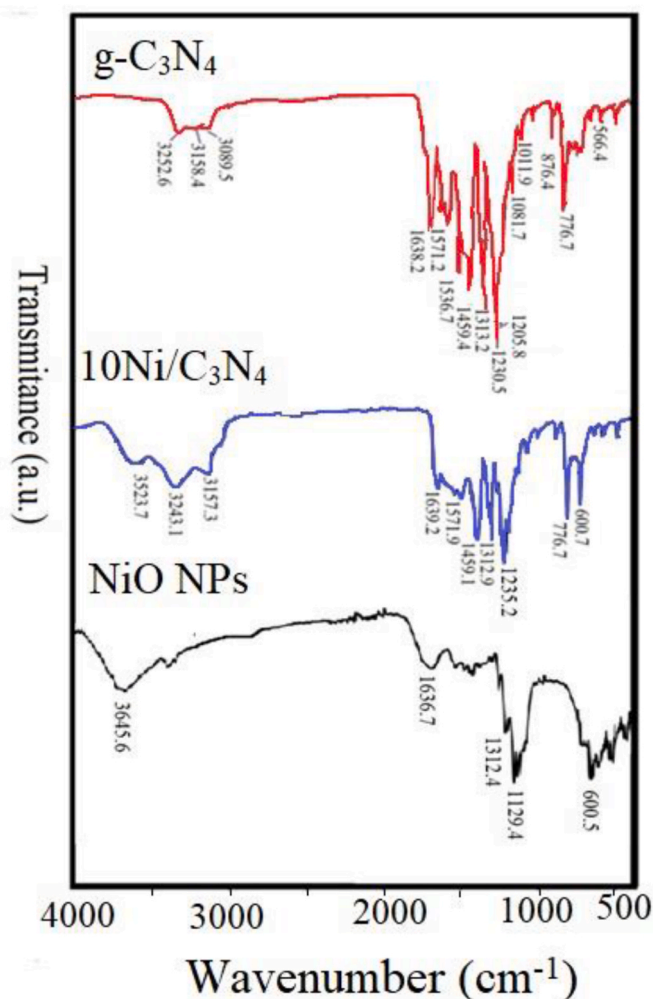
Fig. 4. FTIR spectra of g-C$_3$N$_4$, NiO NPs, and NiO/g-C$_3$N$_4$.

3.2. Photoluminescence and photoelectrochemical measurements

To understand the effects of NiO on the separation of electron−hole pairs in the g-C$_3$N$_4$ nanosheets, the photoluminescence (PL) spectroscopy analysis was performed. The 10Ni/C$_3$N$_4$ was selected as representative of NiO/g-C$_3$N$_4$ samples. As can be seen from the PL spectra in Fig. 10a, the PL spectrum of the samples are in following order C$_3$N$_4$> NiO NPs > NiO/g-C$_3$N$_4$ with the strong peak around 470 nm. The data suggest that NiO/g-C$_3$N$_4$ has a longest lifetime of photogenerated carriers or the lowest recombination rate compared to C$_3$N$_4$ and NiO [32]. In addition, to strengthened that this is related with the improved photocatalytic activities of NiO/g-C$_3$N$_4$, the Nyquist plots from EIS measurement (Fig. 10b) was obtained, which clarify charge-transfer processes at an electrode interface. As shown by the Nyquist plots, the NiO/C$_3$N$_4$ nanocomposite showed the smaller arc radius compared to g-C$_3$N$_4$ suggests the faster charge-transfer efficiency. This should contribute to the improvement on photocatalytic efficiency of the photogenerated electron−hole pairs. The higher-frequency arc in the Nyquist plots of g-C$_3$N$_4$ may be related to the reduction in charge transfer, which is attributed to the double-layer capacitance (Cdl) and charge-transfer resistance (Rct) at the contact interface between the electrode and electrolyte solution [33,34].

3.3. Photocatalytic activity

The photocatalytic activity of the NiO/C$_3$N$_4$ samples was investigated in RhB and TC photocatalytic degradation under visible light. Fig. 11a presents the kinetics of RhB degradation over NiO/C$_3$N$_4$ samples compared to the process using g-C$_3$N$_4$ samples and NiO NPs. It is seen that the larger degradation rate achieved by NiO/g-C$_3$N$_4$ samples compared to both NiO NPs and g-C$_3$N$_4$ corresponding to the synergistic photoactivity created by the combination of NiO and g-C$_3$N$_4$ in the nanocomposite. From the initial change of RhB and the DE values, it is seen that pristine g-C$_3$N$_4$ showed a poor photocatalytic activity as there is about 7.4 ppm/h of the initial rate value, and
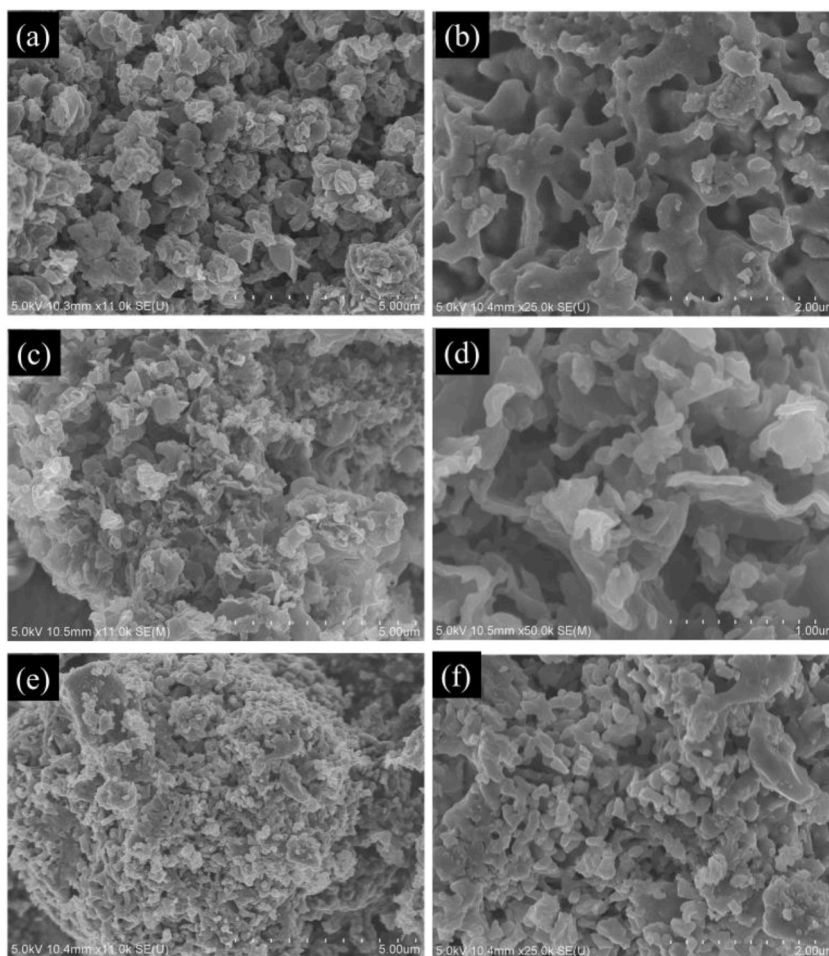
Fig. 5. SEM images of (a–b) g-C$_3$N$_4$ (c–d) 5Ni/C$_3$N$_4$, and (e–f) 20Ni/C$_3$N$_4$ with different magnifications.

Table 1
EDX analysis results of g-C$_3$N$_4$ and NiO/g-C$_3$N$_4$ samples.

Element	Percentage (% wt.)			
	g-C$_3$N$_4$	5NiO/C$_3$N$_4$	10NiO/C$_3$N$_4$	20NiO/C$_3$N$_4$
C	33.95	20.59	20.12	23.02
N	63.83	60.77	59.21	46.10
O	2.22	10.91	9.92	9.59
Ni	–	6.91	10.01	23.27

30% of degradation efficiency achieved for 2 h of treatment, meanwhile other samples exhibit the initial rate of 3.4–4.6 that of g-C$_3$N$_4$ and the DE of more than 80% at the same time. Moreover, by varied Ni content in the nanocomposite, the DE values are in following order: 10Ni/C$_3$N$_4$ > 20Ni/C$_3$N$_4$ > 5Ni/C$_3$N$_4$. Even though the DE achieved by NiO NPs is higher compared to g-C$_3$N$_4$, the initial rate expressed by NiO/C$_3$N$_4$ samples are at about 1.7–2.4 times that of NiO NPs. Moreover, photoactivity of the nanocomposite seems to be correlated with the band gap energy and the absorptive capability of the materials as represented by UV-DRS analysis. The data suggest that the enhanced photoactivity is owing to the reduced recombination of photogenerated electron-hole pairs by combining the NiO and g-C$_3$N$_4$ band gap energy level. Furthermore, from the kinetic evaluation, it is concluded that the RhB degradation over NiO/C$_3$N$_4$ samples obey pseudo-second order kinetic equation as stated by following equation (eq. (2)):

$$\frac{1}{[RhB]_t} = \frac{1}{[RhB]_0} + kt \tag{2}$$

The pseudo-second order kinetics of RhB degradation is presented in Fig. 11c. Meanwhile, the degradation kinetics over NiO NPs and g-C$_3$N$_4$ samples are fit to the pseudo-first order equation with following equation:

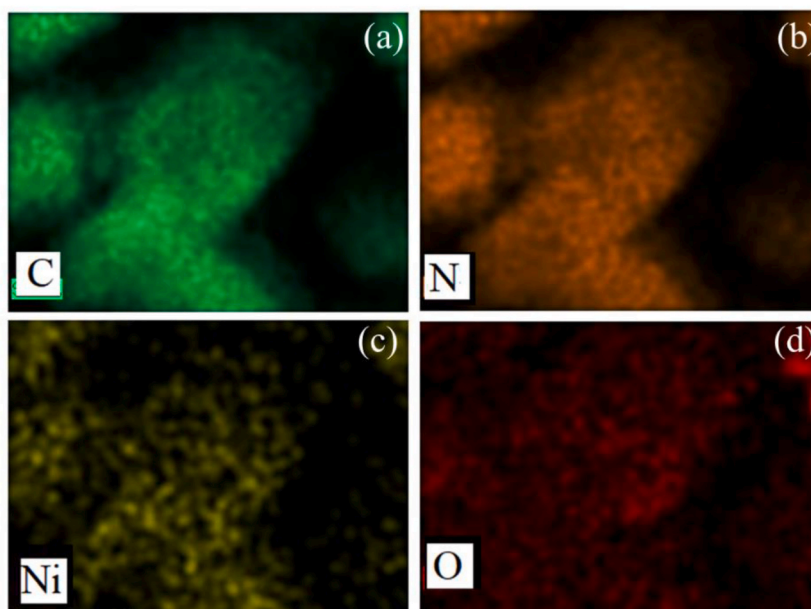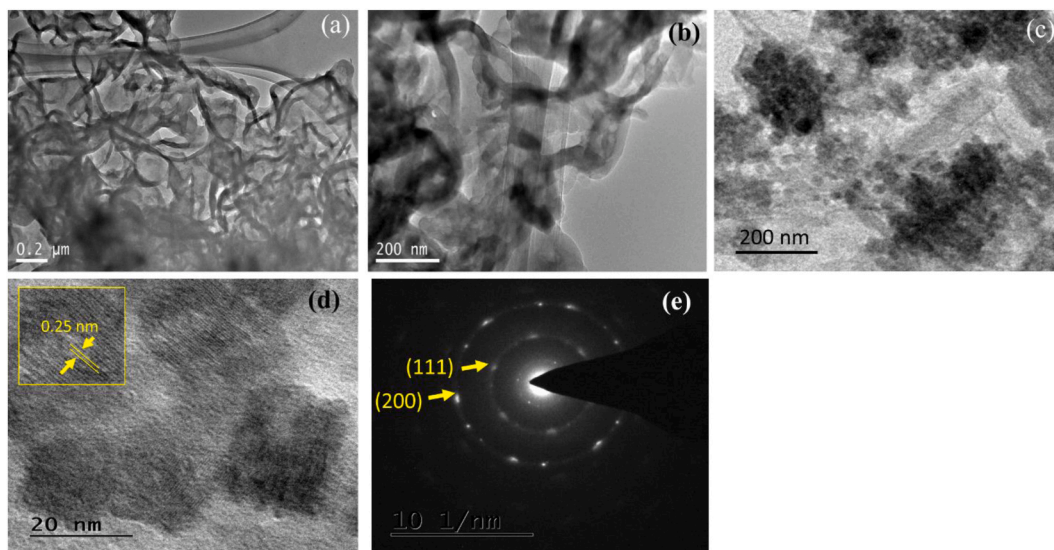Fig. 6. EDX mapping of (a) C, (b) N, (d) Ni, and (d) O- in NiO/g-C$_3$N$_4$ sample (10Ni/C$_3$N$_4$).

Fig. 7. TEM images of (a–b) g-C$_3$N$_4$, (c–d) TEM image of 20Ni/C$_3$N$_4$ with different magnifications, (e). SAED pattern of 20Ni/C$_3$N$_4$.

$$ln \frac{[RhB]_0}{[RhB]_t} = kt \tag{3}$$

where $[RhB]_0$ and $[RhB]_t$ are initial concentration of RhB and the concentration at time of t, respectively, and k is the kinetics constant. The higher order represents the significant role of the photocatalyst in producing radicals for propagation steps of the oxidation reaction. In addition, the significance role of photocatalysis is reflected by the low or unappreciable RhB removal over adsorption process (Fig. 11d). This suggests that the oxidation mechanism occurs over the presence of both photocatalytic active component and the photon exposure is dominant. There is no such significant difference among the adsorption capacity of the varied samples. Considering the NiO as photocatalytic active in NiO/C$_3$N$_4$ samples, the turn over number (TON) of the process was calculated by using following equation (eq. (4)):

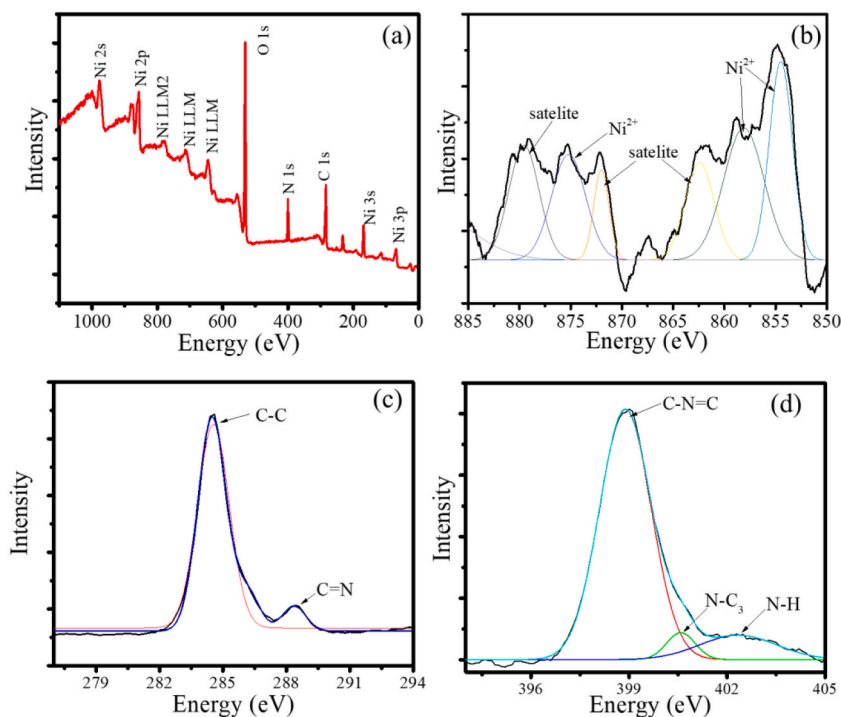$$TON = \frac{Removal\ (\%)}{NiO\ (\%)} \tag{4}$$

Fig. 8. (a) Survey scan of NiO/g-C$_3$N$_4$ (b) Deconvoluted Ni 2p spectrum (c) Deconvoluted C 1s spectrum, (d) Deconvoluted N 1s spectrum.
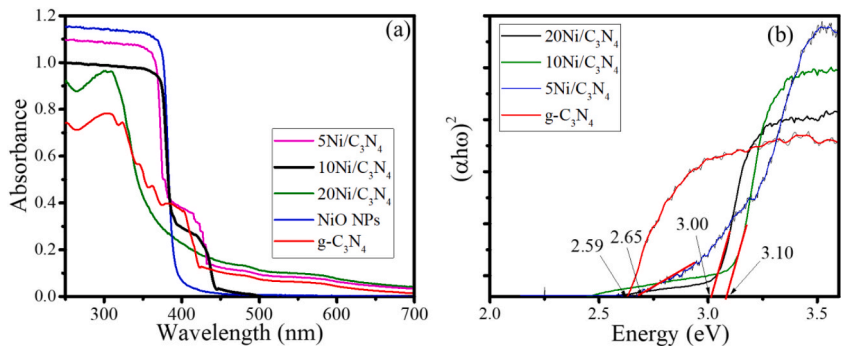

Fig. 9. a. UV-DRS absorption spectra, and (b) Tauc's plot of materials.
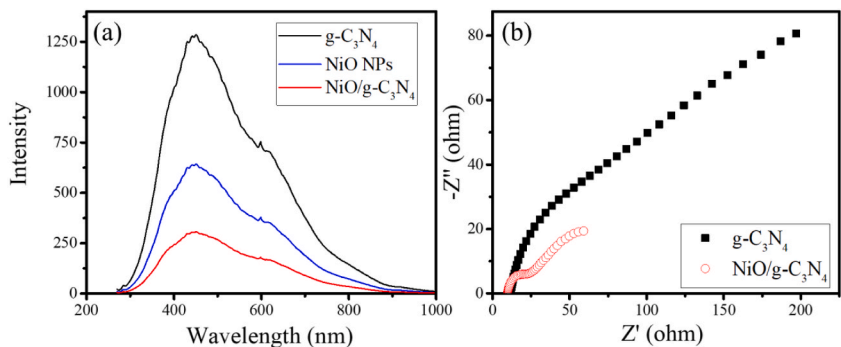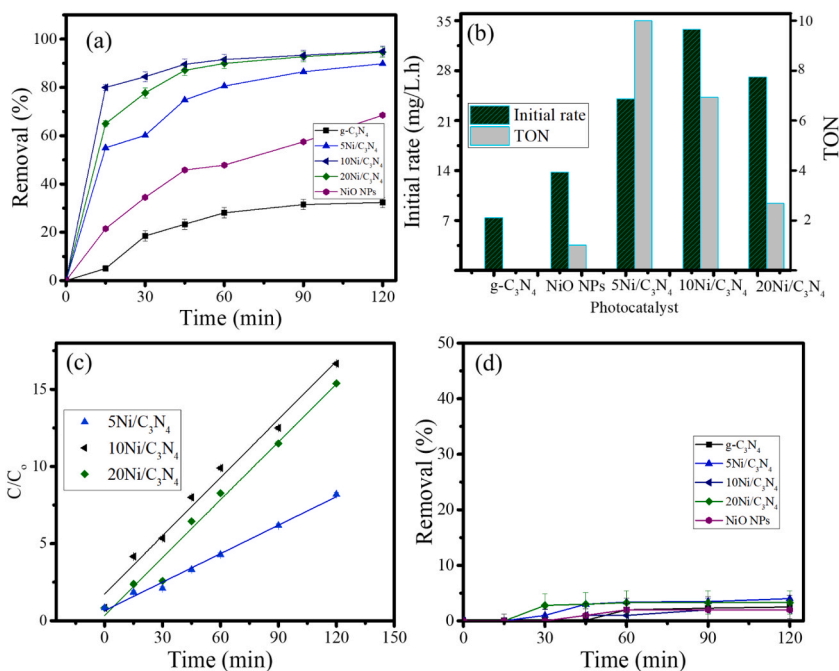

Fig. 10. a. PL spectra, and (b) EIS spectra of materials.

Fig. 11. (a). Kinetics of RhB degradation by the prepared samples, (b). Comparison on the initial rate of RhB degradation, (c) pseudo-second order plot of RhB degradation over NiO/g-C$_3$N$_4$ samples (d) Kinetics of RhB adsorption by the prepared samples.

From Fig. 11b, it is seen that the highest TON is achieved by 5Ni/C$_3$N$_4$ considering that the effective photocatalytic activity occurred at the lowest amount of NiO in the nanocomposite, relative to other NiO/g-C$_3$N$_4$ samples.

Similar trend in the increasing photoactivity by NiO/g-C$_3$N$_4$ samples compared to NiO and g-C$_3$N$_4$ is reflected in the photocatalytic activity test towards TC (Fig. 12 a and 12 b). The kinetics plot and the fitness of the kinetics data to pseudo-second order kinetics are presented in Fig. 12 a and 12c. Similar with in RhB, the kinetics of TC photodegradation over NiO and C$_3$N$_4$ samples follow the pseudo-
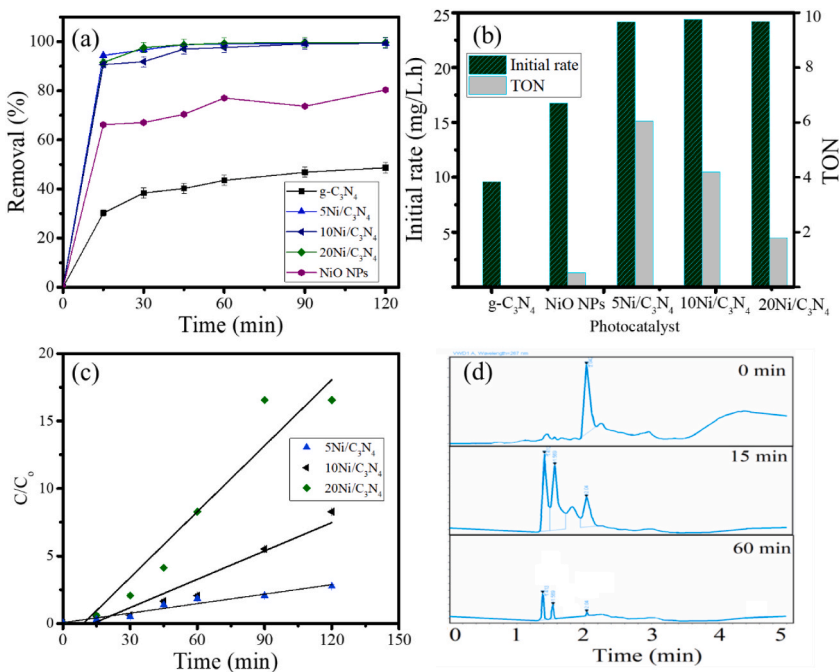
Fig. 12. (a). Kinetics of TC degradation by the prepared samples, (b). Compared initial rate of TC degradation, (c) pseudo-second order plot of TC degradation over NiO/g-C$_3$N$_4$ samples, (d) HPLC analysis results to the initial and treated TC solutions.
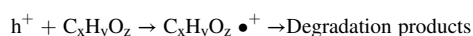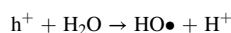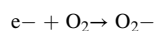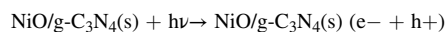
first order kinetics, representing that the crucial change in the kinetics and mechanism occurred by the presence of NiO in the nanocomposite. In general, the photocatalytic activities of NiO/g-C$_3$N$_4$ samples are in similar order with the trend in RhB photodegradation, however, it is seen that faster reaction rate is expressed on TC degradation. The possible reason for this probably related with the smaller molecular size of TC than RhB. From the interpretation of Fig. 12b, it is seen that different with RhB photodegradation data on the initial rate, TC removal shows appreciable enhancement on initial rate data with insignificant different for all NiO/g-C$_3$N$_4$ samples, which gave the values at the range of 24 mg/L/min. However, the TON data expresses similar pattern with in RhB photodegradation, which the highest efficiency is expressed by 5Ni/C$_3$N$_4$·In addition, Fig. 12d provides the fact that there was degradation mechanism rather than adsorption mechanism toward TC as from HPLC analysis, the degradation products are identified instead of the TC as the target molecule. The initial TC solution shows single peak as representation of TC in the solution with the retention time of 2.04 min. After were treated for 15 and 60 min, the associated peak area was decreased along with the formation of other peaks at lower retention time, indicating the degradation products with lower molecular weight.

3.4. Photocatalytic mechanism

Evaluation on the mechanism of photocatalytic oxidation was performed by examined the kinetics of reaction under various scavengers. For this purpose, the addition of IPR, BQ, and EDTA were examined as radicals (•OH), •O$_2$, and hole (h$^+$) scavenger, respectively. Fig. 13 shows the initial rate of the RhB and TC photocatalytic oxidation at varied condition. It is seen that for both target molecules, the addition of IPR and BQ significantly reduce the initial rate, meanwhile, even though not very significant in RhB photocatalytic oxidation, EDTA accelerate the reaction. In more detail, BQ suppressed the initial rate higher compared to IPR, indicating that •O$_2$ plays a relatively important part in the photocatalytic mechanism of both target molecules. The inhibited reaction rate by IPR addition occurred due to the trapping of radicals formed by the excitation produced by the interaction between photoactive site and photon so the propagation steps is diminished. Contrarily, the presence of EDTA in the reaction system block the hole causing slower recombination of electrons and holes. This leads to the actively electron migration to the surface of the photocatalyst for furthermore react with O$_2$ to form HOO• [35]. In addition, the diminished •O$_2$ in the reaction system inhibits the propagation steps of the oxidation mechanism, which conclusively indicating the role of charge transfer process. It is noted that the formed •OH, •O$_2$ and h$^+$ take part in photodegradation system, and consistence with the Z-scheme charge transfer system [36].

It is concluded that either the electron transferred from the CB or the interaction of hole in VB can oxidize adsorbed species. When the photocatalyst absorb light, the electrons in the VB will be excited to their CB producing the holes in the VB. The radicals and super radical electrons will be produced by the interaction of both CB and VB with ambient O$_2$ and radical •OH released by the interacted H$_2$O$_2$ oxidant with light. The mechanism can be stated as follow:

NiO/g-C$_3$N$_4$(s) + hν→ NiO/g-C$_3$N$_4$(s) (e− + h+)

e− + O$_2$→ O$_2$−

h$^+$ + H$_2$O → HO• + H$^+$

h$^+$ + C$_x$H$_y$O$_z$ → C$_x$H$_y$O$_z$ •$^+$ →Degradation products

The photocatalytic degradation mechanism by NiO/g-C$_3$N$_4$ nanocomposite is described by VB and CB of both NiO and g-C$_3$N$_4$. The VB maximum and CB minimum positions of g-C$_3$N$_4$lie at ~1.58 eV and ~ −1.01 eV respectively. As the valence band (VB) and conduction band (CB) edge positions of NiO calculated using Butler-Ginley equation, Eq. (5), and (6) these are respectively 3.00 and −0.28 eV.

$$E_{VB} = \text{X- } E_e + 0.5 \text{ Eg} \tag{5}$$

$$E_{CB} = E_{VB} - \text{Eg} \tag{6}$$

where, E$_{VB}$ and E$_{CB}$ are the VB and CB edge potentials respectively, E$_e$ is the energy of free electrons on the hydrogen scale, and X refers to the absolute Mulliken electronegativity of NiO [7,37].

Refer to the identification of the effect of scavenger, E$_{vB}$ and E$_{CB}$ values of NiO and g-C$_3$N$_4$, the photodegradation process follows Z-scheme mechanism as represented in Fig. 14. The hypothesis is referred to that the CB potential of g-C$_3$N$_4$ is more negative than the reduction potential of O$_2$ while the VB potential of NiO is more positive than the oxidation potential of H$_2$O to · OH. The excited electrons would thermodynamically transfer from the CB of NiO to the VB of g-C$_3$N$_4$. The combined CB electrons of NiO and VB holes of g-C$_3$N$_4$ will have enough thermodynamic energy to induce the reduction in adsorbed O$_2$ and form · O$_2$•−. Conclusively, the heterojunction construction of g-C$_3$N$_4$with NiO is beneficial for accelerating charge migration rate, increasing surface active sites, and then promoting photocatalytic activity.

3.5. Effect of pH

Effect of initial pH of target solution on the kinetics of the photocatalytic oxidation was studied, and the resulted plots is presented in Fig. 15a. As can be seen from two different target; RhB and TC, there is different pattern of pH effect to the initial rate of reaction. The degradation of RhB exhibits the optimum reaction rate at neutral pH (7) and tends to decrease at the lower and higher pH. Contrarily, the optimum pH for TC photodegradation is obtained at pH 10. This different phenomenon represents the different
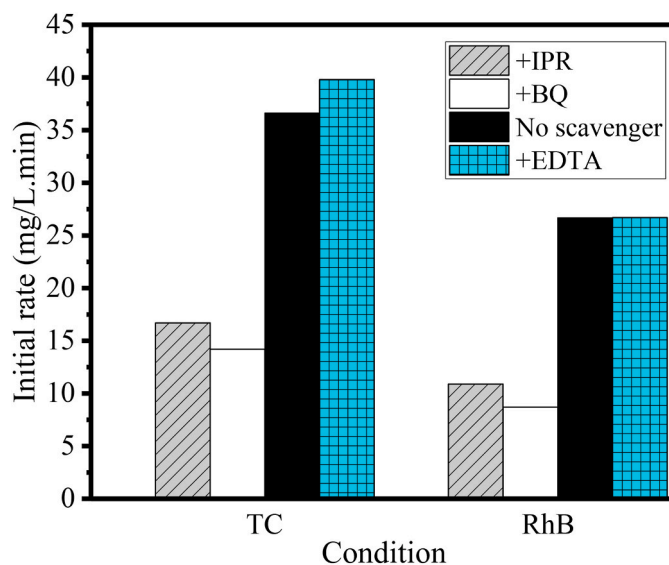
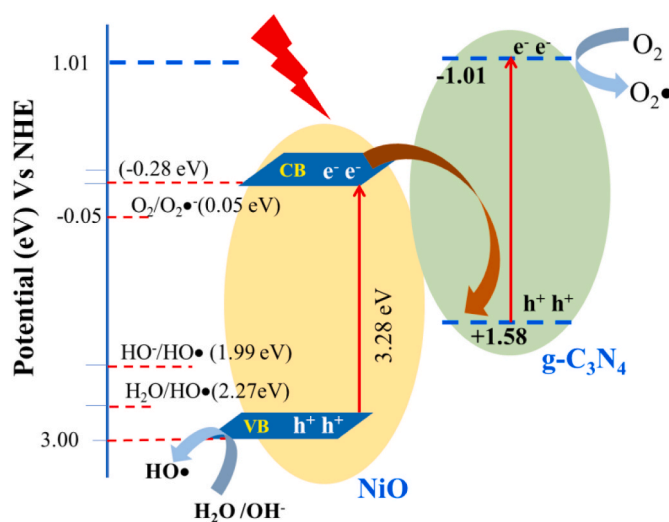**Fig. 13.** Effect of scavengers on initial rate of RhB and TC degradation.

Fig. 14. Z-scheme mechanism in NiO/g-C$_3$N$_4$ photocatalysis.

molecular interaction occurred during the adsorption of molecule onto the NiO/g-C$_3$N$_4$ photocatalysts. As a neutral molecule, the oxidation reaction to TC is controlled by the presence of radicals in the reaction system. The increased alkaline condition contributes to provide more hydroxyl ions that can be converted into hydroxy radicals. However, at the enhanced basicity to pH 11, the provided alkaline condition tends to terminate the radicals via recombination. Similar effect of acidity/basicity on the TC oxidation was also reported by ozonization [38], and photocatalytic oxidation of TC over titanium dioxide [39]. From other side, the RhB photo-degradation tends to decrease in basic pH. From the net positive charge availability in RhB, the photodegradation rate is strongly correlated with the adsorption/desorption and electrostatic effect between the photocatalyst surface and the molecule. At low pH, the photocatalyst surface will be more positive, which contributes to inhibit surface interaction by electrostatic repulsion. In other side, the high alkalinity will provide more –OH that also reduce the interaction of RhB with surface by neutralizing RhB structure. In addition, the RhB tends to form aggregation or dimer molecule which is more difficult to bind to the surface and pore structure of the photo-catalyst [40]. From the measurement, the zero point charges of the photocatalysts surface are within the range of 6.2–7.2, suggesting that the photocatalyst should be active at neutral pH.

3.6. Photocatalyst stability

Recycling and stability of Ni/g-C$_3$N$_4$ was studied by evaluating the DE of photocatalytic process using fresh and recycled
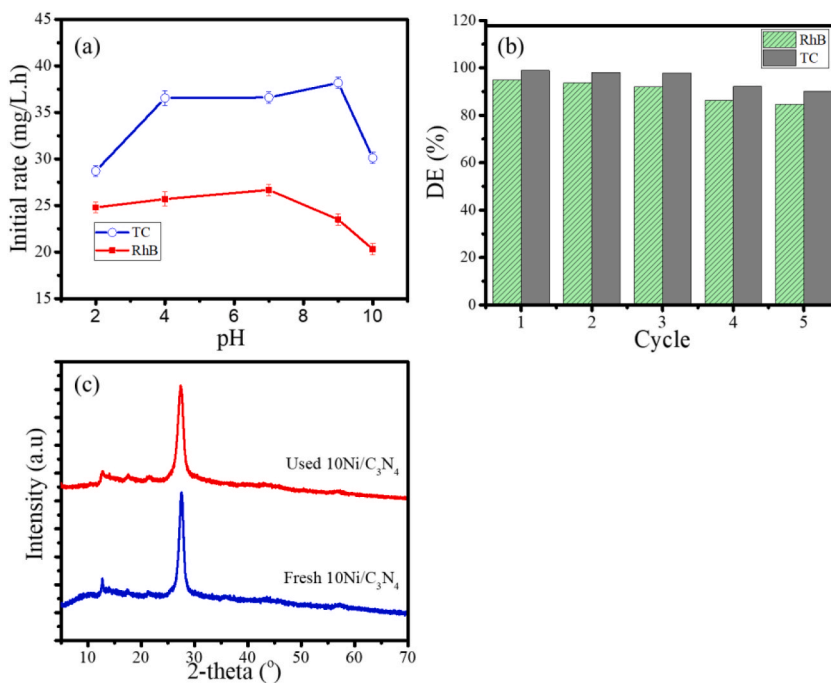
Fig. 15. (a). Effect of pH on initial rate of RhB and TC degradation, (b) DE changes on fresh and reused 10NiO/C_3N_4 photocatalyst, (c) Comparison on XRD pattern of fresh and reused 10NiO/C_3N_4 photocatalyst.

photocatalyst. The 10Ni/C_3N_4 sample was chosen as the representative photocatalyst. The recycling was conducted by washing the used catalyst with ethanol followed by drying in oven at 100 °C overnight. From the graph presented in Fig. 15b, it is seen that the DE values of RhB and TC was found to be reproducible up to five cycles. Even though the slight reduction in DE in third cycle was appeared from both target molecules, the declined DE values are less than 10%. The DE of RhB degradation changes from 95% in first usage into 84.7% in 5th cycle, meanwhile from TC degradation the change is from 98.9% into 90%, respectively. Further investigation using XRD analysis revealed that there are no structural changes observed after 5th usage, suggesting that the prepared nanocomposites are stable and recyclable for practical usage (Fig. 15c).

The photocatalytic activity of NiO/g-C_3N_4 prepared in this work is compared with other NiO-based photocatalysts. From various previous papers, it can be summarized that the photocatalytic activity from this work towards TC degradation is lower compared with NiO/rGO which demonstrated the high DE (99%) in 30 min [41], but comparable respect to the activity of NiO NPs and NiO/CuO nanocomposite, ZnO/NiFe$_2$O$_4$/Co$_3$O$_4$VO$_4$,/NiFe$_2$O$_4$ and NiAl-LDH [42–45]. From RhB photocatalytic oxidation experiment, the activity of this work is also less than NiAl-LDH [42], but comparable with the activity of graphene oxide/Fe$_3$O$_4$/NiO [46], and MoS$_2$/NiS$_2$ [47]. The higher photoactivity is mainly related with the porous structure of NiAl-LDH and NiO/rGO which leads to the increasing adsorptivity for supporting the degradation mechanism.

4. Conclusion

Nanocomposites of NiO/g-C_3N_4 were successfully synthesized by using nickel nanoparticles prepared using *Tinosphora cordifolia* stem extract. Physicochemical characterization to the nanocomposites revealed the homogeneously distributed NiO NPs with the enhanced photocatalytic activity of the nanocomposite in visible light range achieved. From the study on the effect of varied Ni content, it is found that the photocatalytic activity is related with the band gap energy and particle size of NiO NPs in the nanocomposite. The experimental results demonstrated that NiO/g-C_3N_4 Z-scheme heterojunctions exhibited excellent photocatalytic degradation activity of RhB and TC under visible light irradiation. The degradation efficiency reached 95% and 98% for RhB and TC for 60 min of treatment, respectively.

Author contribution statement

Is Fatimah: Conceived and designed the experiments; Analyzed and interpreted the data; Wrote the paper.

Rizky Zenita Sulstiyowati: Performed the experiments; Analyzed and interpreted the data; Contributed reagent, materials, analysis data.

Aditytia Wijayana, Gani Purwiandono, Suresh Sagadevan: Performed the experiments; Contributed reagents, materials, analysis tools or data; Wrote the paper.

Data availability statement

Data will be made available on request.

Funding statement

Declaration of competing interest

The authors declare that they have no known competing financial interests or personal relationships that could have appeared to influence the work reported in this paper.

References

[1] R. Al-Tohamy, S.S. Ali, F. Li, K.M. Okasha, Y.A.G. Mahmoud, T. Elsamahy, H. Jiao, Y. Fu, J. Sun, A critical review on the treatment of dye-containing wastewater: ecotoxicological and health concerns of textile dyes and possible remediation approaches for environmental safety, Ecotoxicol. Environ. Saf. 231 (2022), 113160, https://doi.org/10.1016/j.ecoenv.2021.113160.

[2] D. Ma, H. Yi, C. Lai, X. Liu, X. Huo, Z. An, L. Li, Y. Fu, B. Li, M. Zhang, L. Qin, S. Liu, L. Yang, Critical review of advanced oxidation processes in organic wastewater treatment, Chemosphere 275 (2021), 130104, https://doi.org/10.1016/j.chemosphere.2021.130104.

[3] C. Zhao, L. Cai, K. Wang, B. Li, S. Yuan, Z. Zeng, L. Zhao, Y. Wu, Y. He, Novel Bi2WO6/ZnSnO3 heterojunction for the ultrasonic-vibration-driven piezocatalytic degradation of RhB, Environ. Pollut. 319 (2023), 120982.

[4] L. Chen, W. Zhang, J. Wang, X. Li, Y. Li, X. Hu, L. Zhao, Y. Wu, Y. He, High piezo/photocatalytic efficiency of Ag/Bi5O7I nanocomposite using mechanical and solar energy for N2 fixation and methyl orange degradation, Green Energy Environ 8 (2021) 283–295, https://doi.org/10.1016/j.gee.2021.04.009.

[5] I. Fatimah, G. Fadillah, I. Yanti, R. Doong, Clay-supported metal oxide nanoparticles in catalytic advanced oxidation processes: a review, Nanomaterials 15 (2022) 825.

[6] H. Li, S. Yin, T. Sato, Y. Wang, Enhanced photocatalytic performance of luminescent g-C3N4 photocatalyst in darkroom, Nanoscale Res. Lett. 11 (2016) 1–9, https://doi.org/10.1186/s11671-016-1303-2.

[7] K. Qi, A. Zada, Y. Yang, Q. Chen, A. Khataee, Design of 2D–2D NiO/g-C3N4 heterojunction photocatalysts for degradation of an emerging pollutant, Res. Chem. Intermed. 46 (2020) 5281–5295, https://doi.org/10.1007/s11164-020-04262-0.

[8] I. Fatimah, I. Sahroni, O. Muraza, R.-A. Doong, One-pot biosynthesis of SnO2 quantum dots mediated by Clitoria ternatea flower extract for photocatalytic degradation of rhodamine B, J. Environ. Chem. Eng. 8 (2020), 103879.

[9] D. Singh, P.K. Chaudhuri, Chemistry and pharmacology of Tinospora cordifolia, Nat. Prod. Commun. 12 (2017) 299–308, https://doi.org/10.1177/1934578x1701200240.

[10] M. Saeed, M. Naveed, J. Leskovec, A. Ali kamboh, I. Kakar, K. Ullah, F. Ahmad, M. Sharif, A. Javaid, M. Rauf, M.E. Abd El-Hack, M.A. Abdel-Latif, S. Chao, Using Guduchi (Tinospora cordifolia) as an eco-friendly feed supplement in human and poultry nutrition, Poultry Sci. 99 (2020) 801–811, https://doi.org/10.1016/j.psj.2019.10.051.

[11] G.C. Jagetia, S.K. Rao, Evaluation of the antineoplastic activity of guduchi (Tinospora cordifolia) in Ehrlich ascites carcinoma bearing mice, Biol. Pharm. Bull. 29 (2006) 460–466, https://doi.org/10.1248/bpb.29.460.

[12] A. Palmieri, L. Scapoli, A. Iapichino, L. Mercolini, M. Mandrone, F. Poli, A.B. Giannì, C. Baserga, M. Martinelli, Berberine and Tinospora cordifolia exert a potential anticancer effect on colon cancer cells by acting on specific pathways, Int. J. Immunopathol. Pharmacol. 33 (2019) 1–10, https://doi.org/10.1177/2058738419855567.

[13] K. Selvam, C. Sudhakar, M. Govarthanan, P. Thiyagarajan, A. Sengottaiyan, B. Senthilkumar, T. Selvankumar, Eco-friendly biosynthesis and characterization of silver nanoparticles using Tinospora cordifolia (Thunb.) Miers and evaluate its antibacterial, antioxidant potential, J. Radiat. Res. Appl. Sci. 10 (2017) 6–12, https://doi.org/10.1016/j.jrras.2016.02.005.

[14] P.C. Nethravathi Udayabhanu, M.A. Pavan Kumar, D. Suresh, K. Lingaraju, H. Rajanaika, H. Nagabhushana, S.C. Sharma, Tinospora cordifolia mediated facile green synthesis of cupric oxide nanoparticles and their photocatalytic, antioxidant and antibacterial properties, Mater. Sci. Semicond. Process. 33 (2015) 81–88, https://doi.org/10.1016/j.mssp.2015.01.034.

[15] I. Fatimah, G. Purwiandono, M. Husnu Jauhari, A. Audita Aisyah Putri Maharani, S. Sagadevan, W.C. Oh, R. an Doong, Synthesis and control of the morphology of SnO2 nanoparticles via various concentrations of Tinospora cordifolia stem extract and reduction methods, Arab. J. Chem. 15 (2022), 103738, https://doi.org/10.1016/j.arabjc.2022.103738.

[16] Z. Mo, X. She, Y. Li, L. Liu, L. Huang, Z. Chen, Q. Zhang, H. Xu, H. Li, Synthesis of g-C3N4 at different temperatures for superior visible/UV photocatalytic performance and photoelectrochemical sensing of MB solution, RSC Adv. 5 (2015) 101552–101562, https://doi.org/10.1039/c5ra19586a.

[17] X. Chen, X. Wang, F. Liu, X. Song, H. Cui, Fabrication of NiO–ZnO-modified g-C3N4 hierarchical composites for high-performance supercapacitors, Vacuum 178 (2020) 3–10, https://doi.org/10.1016/j.vacuum.2020.109453.

[18] Q. Fardiyah, T. Ersam Suyanta, A. Slamet, F. Kurniawan Suprapto, New potential and characterization of Andrographis paniculata L. Ness plant extracts as photoprotective agent, Arab. J. Chem. 13 (2020) 8888–8897, https://doi.org/10.1016/j.arabjc.2020.10.015.

[19] A. Puri, S. Patil, Tinospora cordifolia stem extract-mediated green synthesis of selenium nanoparticles and its biological applications, Pharmacogn. Res. 14 (2022) 289–296, https://doi.org/10.5530/pres.14.3.42.

[20] D. Muñetón Arboleda, J.M.J. Santillán, L.J. Mendoza Herrera, M.B.F. Van Raap, P. Mendoza Zélis, D. Muraca, D.C. Schinca, L.B. Scaffardi, Synthesis of Ni nanoparticles by femtosecond laser ablation in liquids: structure and sizing, J. Phys. Chem. C 119 (2015) 13184–13193, https://doi.org/10.1021/acs.jpcc.5b03124.

[21] I.D. Likasari, R.W. Astuti, A. Yahya, N. Isnaini, G. Purwiandono, H. Hidayat, W.P. Wicaksono, I. Fatimah, NiO nanoparticles synthesized by using Tagetes erecta L leaf extract and their activities for photocatalysis, electrochemical sensing, and antibacterial features, Chem. Phys. Lett. 780 (2021), https://doi.org/10.1016/j.cplett.2021.138914.

[22] Z. Sabouri, N. Fereydouni, A. Akbari, H.A. Hosseini, A. Hashemzadeh, M.S. Amiri, R. Kazemi Oskuee, M. Darroudi, Plant-based synthesis of NiO nanoparticles using salvia macrosiphon Boiss extract and examination of their water treatment, Rare Met. 39 (2020) 1134–1144, https://doi.org/10.1007/s12598-019-01333-z.

[23] A. Upadhyay, K. Kumar, A. Kumar, H. Mishra, Tinospora cordifolia (Willd.) Hook. f. and Thoms. (Guduchi) - validation of the Ayurvedic pharmacology through experimental and clinical studies, Int. J. Ayurveda Res. 1 (2010) 112, https://doi.org/10.4103/0974-7788.64405.

[24] P.W. Citradewi, H. Hidayat, G. Purwiandono, I. Fatimah, S. Sagadevan, Clitorea ternatea-mediated silver nanoparticle-doped hydroxyapatite derived from cockle shell as antibacterial material, Chem. Phys. Lett. 769 (2021), 138412, https://doi.org/10.1016/j.cplett.2021.138412.

[25] A. Hussen, Review on g-C3N4 based fluorescence chemical sensor for detection of heavy metal ions, Asian J. Basic Sci. Res. 3 (2021) 69–84, https://doi.org/10.38177/ajbsr.2021.3106.

[26] M.M. Ba-Abbad, P.V. Chai, M.S. Takriff, A. Benamor, A.W. Mohammad, Optimization of nickel oxide nanoparticle synthesis through the sol-gel method using Box-Behnken design, Mater. Des. 86 (2015) 948–956, https://doi.org/10.1016/j.matdes.2015.07.176.

[27] H.G. Gebretinsae, M.G. Tsegay, Z.Y. Nuru, Biosynthesis of nickel oxide (NiO) nanoparticles from cactus plant extract, Mater. Today Proc. 36 (2019) 566–570, https://doi.org/10.1016/j.matpr.2020.05.331.

[28] F. Ma, Y. Ji, B. Liu, J. Wang, B. Zhou, G. Zhen, F. Long, Z. Zou, Preparation of graphite phase carbon nitride (g-C3N4) micro-nano bouquet by thermal polymerization, Mater. Res. Express 7 (2020), https://doi.org/10.1088/2053-1591/abc4b6.

[29] F.T. Thema, E. Manikandan, A. Gurib-Fakim, M. Maaza, Single phase Bunsenite NiO nanoparticles green synthesis by Agathosma betulina natural extract, J. Alloys Compd. 657 (2016) 655–661, https://doi.org/10.1016/j.jallcom.2015.09.227.

[30] A. Haider, M. Ijaz, S. Ali, J. Haider, M. Imran, H. Majeed, J.A.K. Iram Shahzadi, Muhammad Muddassir Ali, M. Ikram, Green synthesized phytochemically (zingiber officinale and allium sativum) reduced nickel oxide nanoparticles confirmed bactericidal and catalytic potential, Nanoscale Res. Lett. 15 (2020) 2–11.

[31] R.A. Senthil, J. Theerthagiri, A. Selvi, J. Madhavan, Synthesis and characterization of low-cost g-C3N4/TiO2 composite with enhanced photocatalytic performance under visible-light irradiation, Opt. Mater. 64 (2017) 533–539, https://doi.org/10.1016/j.optmat.2017.01.025.

[32] W. Duan, P. Yan, J. Dong, Y. Chen, X. He, J. Chen, J. Qian, L. Xu, H. Li, A self-powered photoelectrochemical aptamer probe for oxytetracycline based on the use of a NiO nanocrystal/g-C3N4 heterojunction, Microchim. Acta 186 (2019), https://doi.org/10.1007/s00604-019-3856-0.

[33] O. Fónagy, E. Szabó-Bárdos, O. Horváth, 1,4-Benzoquinone and 1,4-hydroquinone based determination of electron and superoxide radical formed in heterogeneous photocatalytic systems, J. Photochem. Photobiol. Chem. 407 (2021), https://doi.org/10.1016/j.jphotochem.2020.113057.

[34] D. Wang, J. Li, Z. Xu, Y. Zhu, G. Chen, Z. Cui, Synthesis of g-C3N4/NiO p–n heterojunction materials with ball-flower morphology and enhanced photocatalytic performance for the removal of tetracycline and Cr6+, J. Mater. Sci. 54 (2019) 11417–11434.

[35] A. Nezamzadeh-Ejhieh, H. Zabihi-Mobarakeh, Heterogeneous photodecolorization of mixture of methylene blue and bromophenol blue using CuO-nano-clinoptilolite, J. Ind. Eng. Chem. 20 (2014) 1421–1431, https://doi.org/10.1016/j.jiec.2013.07.027.

[36] B. Li, C. Lai, G. Zeng, L. Qin, H. Yi, D. Huang, C. Zhou, X. Liu, M. Cheng, P. Xu, C. Zhang, F. Huang, S. Liu, Facile hydrothermal synthesis of Z-scheme Bi2Fe4O9/ Bi2WO6 heterojunction photocatalyst with enhanced visible light photocatalytic activity, ACS Appl. Mater. Interfaces 10 (2018) 18824–18836, https://doi.org/ 10.1021/acsami.8b06128.

[37] S. Sadhukhan, A. Bhattacharyya, D. Rana, T.K. Ghosh, J.T. Orasugh, S. Khatua, K. Acharya, D. Chattopadhyay, Synthesis of RGO/NiO nanocomposites adopting a green approach and its photocatalytic and antibacterial properties, Mater. Chem. Phys. 247 (2020), 122906, https://doi.org/10.1016/j. matchemphys.2020.122906.

[38] J. Wu, Y. Jiang, L. Zha, Z. Ye, Z. Zhou, J. Ye, H. Zhou, Tetracycline degradation by ozonation, and evaluation of biodegradability and toxicity of ozonation byproducts, Can. J. Civ. Eng. 37 (2010) 1485–1491, https://doi.org/10.1139/L10-100.

[39] G.H. Safari, M. Hoseini, M. Seyedsalehi, H. Kamani, J. Jaafari, A.H. Mahvi, Photocatalytic degradation of tetracycline using nanosized titanium dioxide in aqueous solution, Int. J. Environ. Sci. Technol. 12 (2015) 603–616, https://doi.org/10.1007/s13762-014-0706-9.

[40] S.D. Khairnar, V.S. Shrivastava, Facile synthesis of nickel oxide nanoparticles for the degradation of Methylene blue and Rhodamine B dye: a comparative study, J. Taibah Univ. Sci. 13 (2019) 1108–1118, https://doi.org/10.1080/16583655.2019.1686248.

[41] I. Fatimah, P. Widya, G. Purwiandono, H. Hidayat, Nickel oxide decorated reduced graphene oxide synthesized using single bioreductor of Pometia pinnata leaves extract as photocatalyst in tetracycline photooxidation and antibacterial agent, Inorg. Chem. Commun. 148 (2023), 110287, https://doi.org/10.1016/j. inoche.2022.110287.

[42] X. Song, S. Ye, X. Zhou, W. Gui, C. Yang, Z. Yang, Construction of Z-scheme NiO/NiC/g-C3N4composites using NiC as novel cocatalysts for the efficient photocatalytic degradation, RSC Adv. 11 (2021) 24822–24835, https://doi.org/10.1039/d1ra03562b.

[43] H. Ahsan, M. Shahid, M. Imran, F. Mahmood, M.H. Siddique, H.M. Ali, M.B.K. Niazi, S. Hussain, M. Shahbaz, M. Ayyub, T. Shahzad, Photocatalysis and adsorption kinetics of azo dyes by nanoparticles of nickel oxide and copper oxide and their nanocomposite in an aqueous medium, PeerJ 10 (2022), e14358, https://doi.org/10.7717/peerj.14358.

[44] N. Sreeram, V. Aruna, R. Koutavarapu, D. Lee, J. Shim, Novel indium vanadium oxide nanosheet-supported nickel iron oxide nanoplate heterostructure for synergistically enhanced photocatalytic degradation of tetracycline, Catalysts 12 (2022), 12111471, https://doi.org/10.3390/catal12111471.

[45] M. Doosti, R. Jahanshahi, S. Laleh, S. Sobhani, J.M. Sansano, Solar light induced photocatalytic degradation of tetracycline in the presence of ZnO/NiFe2O4/ Co3O4 as a new and highly efficient magnetically separable photocatalyst, Front. Chem. 10 (2022) 1–17, https://doi.org/10.3389/fchem.2022.1013349.

[46] T. Saleem, R.A. Sarfaraz, I. Ahmed, H. Zulfiqar, Y. Iqbal, I. Saeed, M. Ashraf, U. Anwar, Synthesis and characterization of nanostructured ternary composites of graphene oxide/Fe3 O4/NiO for waste water treatment, Dig. J. Nanomater. Biostruct. 17 (2022) 1203–1210, https://doi.org/10.15251/DJNB.2022.174.1203.

[47] S. Harish, P. Bharathi, P. Prasad, R. Ramesh, S. Ponnusamy, M. Shimomura, J. Archana, M. Navaneethan, Interface enriched highly interlaced layered MoS2/ NiS2nanocomposites for the photocatalytic degradation of rhodamine B dye, RSC Adv. 11 (2021) 19283–19293, https://doi.org/10.1039/d1ra01941d.